# Electron Microscopy Study of the "Cubic" Perovskite Phase SrFe$_{1-x}$V$_x$O$_{2.5+x}$ (0.05 $\leq$ $x$ $\leq$ 0.1)

N. NAKAYAMA* AND M. TAKANO

*Institute for Chemical Research, Kyoto University, Uji, Kyoto-fu 611, Japan*

S. INAMURA† AND N. NAKANISHI

*Department of Chemistry, Faculty of Science, Konan University, Motoyama, Kobe 658, Japan*

AND K. KOSUGE

*Department of Chemistry, Faculty of Science, Kyoto University, Kyoto 606, Japan*

The oxygen-deficient "cubic" perovskite phase SrFe$_{1-x}$V$_x$O$_{2.5+x}$ (0.05 $\leq$ $x$ $\leq$ 0.10) quenched from 1473 K has been investigated by electron microscopy. Samples show a microdomain structure composed of ordered grains less than 20 nm. Oxygen vacancies form a brownmillerite-type superlattice in each microdomain, while six orientation variants have been observed within a particle; the oxygen vacancies in one domain are stringed along one of the six possible $\langle 110 \rangle_c$ directions of the cubic host lattice. The domain size decreases as $x$ or oxygen content increases. Vacancy arragements within the domains observed in high-resolution lattice images indicate that good structural coherence exists between microdomains and that a basic cubic perovskite skeleton is framed throughout a particle; they also suggest that vacancy content decreases in the boundary regions. © 1987 Academic Press, Inc.

## Introduction

The structure of oxygen-deficient perovskites, generally formulated as $ABO_{3-x}$, has been widely investigated. At lower concentrations, vacancies tend to be randomly distributed at the oxide ion sites, while at higher concentrations, most of these oxides form superstructures because of vacancy ordering. Nevertheless, several highly deficient phases like SrVO$_{2.5}$ (*1*) that give powder X-ray diffraction (XRD) patterns of cubic symmetry suggesting randomized vacancy distribution have been reported. More recently, short-range ordering in the form of microdomains has been reported by Alario-Franco et al. (*2–7*).

SrFeO$_{2.5}$ or Sr$_2$Fe$_2$O$_5$ is well known to have an orthorhombic, brownmillerite-type structure which can be derived from the cubic perovskite-type structure of SrFeO$_3$ by removing one-sixth of the oxygen atoms

---

* To whom correspondence should be addressed.
† Present address: Osaka Prefectural Industrial Research Institute, Osaka 550, Japan.

in an ordered way (8, 9); however, Shin *et al.* (10) found that the ordering was destroyed at elevated temperatures. A catalytic activity to decompose NO into $N_2$ and $O_2$ found in the cubic phase (11), initiated by a step of adsorbing NO molecules at the vacancy sites, was assumed to be enhanced by the randomized vacancy distribution. We have attempted to stabilize this interesting phase for characterization by structural and physical measurements. Although even a very rapid cooling at $>10^6$ K sec$^{-1}$ from the molten state was of no use, we found that slight substitution of $V^{5+}$ ions for the $Fe^{3+}$ ions made it possible to quench a cubic phase rather easily. In this paper we describe the results of phase analysis and microstructural study of the "cubic" perovskite system $SrFe_{1-x}V_xO_{2.5+x}$.

## Experimental

Samples were prepared by the reaction of $Sr_2Fe_2O_5$, $Sr_3V_2O_8$, and $V_2O_5$ powders. $Sr_2Fe_2O_5$ was obtained by firing $SrCO_3$ and $Fe_2O_3$ under evacuation to 0.1 Pa at 1273 K and firing the product again under the same conditions after grinding and mixing. The quenched brown powder was examined by XRD and Mössbauer spectroscopy. $Sr_3V_2O_8$ was obtained by the same method but in the air from $SrCO_3$ and $V_2O_5$. All the raw materials used $SrCO_3$, $Fe_2O_3$, and $V_2O_5$, had nominal purities above 99.9% (Furuuchi Chemicals). Mixtures of $Sr_2Fe_2O_5$, $Sr_3V_2O_8$, and $V_2O_5$ held in platinum containers were sealed in evacuated quartz tubes, heated for 16 hr at 1473 K, and subsequently quenched from 1473 K, grounded, and mixed. This reaction process was repeated three times to obtain homogeneous single-phase products. The nominal composition of $SrFe_{1-x}V_xO_{2.5+x}$ ranged from $x = 0.0$ to 0.2. The oxygen composition was determined by assuming

trivalent iron atoms as confirmed by the Mössbauer spectra and pentavalent vanadium atoms.

Phase identification was performed mainly by powder X-ray diffraction (XRD). CuKα radiation from a rotating anode-type X-ray generator (Rigaku RU-200) was used for the measurements. The diffracted X-ray beams were monochromated with a pyrolytic graphite crystal to reduce the fluorescent X-rays. Electron diffraction (ED) patterns and lattice images were obtained by using JEM-100CX and JEM-200CX electron microscopes. Samples were crushed and dispersed in ethyl alcohol, and thin crystalline fragments were collected on a holey microgrid coated with a thin carbon film.

## Observations and Interpretation

### X-ray Powder Diffraction Pattern

Figure 1 shows the variation of the powder XRD patterns near the $(220)_C$ or $(282)_B$ reflection with composition $x$. Hereafter, the subscript "c" refers to the cubic perovskite cell and subscript "b" to the brownmillerite-type orthorhombic cell with $Ibm2$ symmetry (9). These cells are related to each other as $a_B$, $c_B = 2^{1/2}a_C$ and $b_B = 4a_C$, $[100]_B$ and $[001]_B$ being almost parallel to $[110]_C$ and $[1\bar{1}0]_C$, respectively. The oxygen vacancies are stringed along $[001]_B$ in the orthorhombic structure. Sample $x = 0.01$ shows a pattern quite similar to that of $Sr_2Fe_2O_5$ and the lattice parameters remain almost the same, whereas samples $x = 0.016$ and 0.03 show broadened diffraction lines manifesting serious effects of the substitution on the structure. With increasing $x$, the basic reflections become sharper and stronger, while superlattice reflections become broader. The full width at half-maximum (FWHM) of the basic reflections almost reaches the instrumental resolution for $x > 0.05$. The appearance of weak
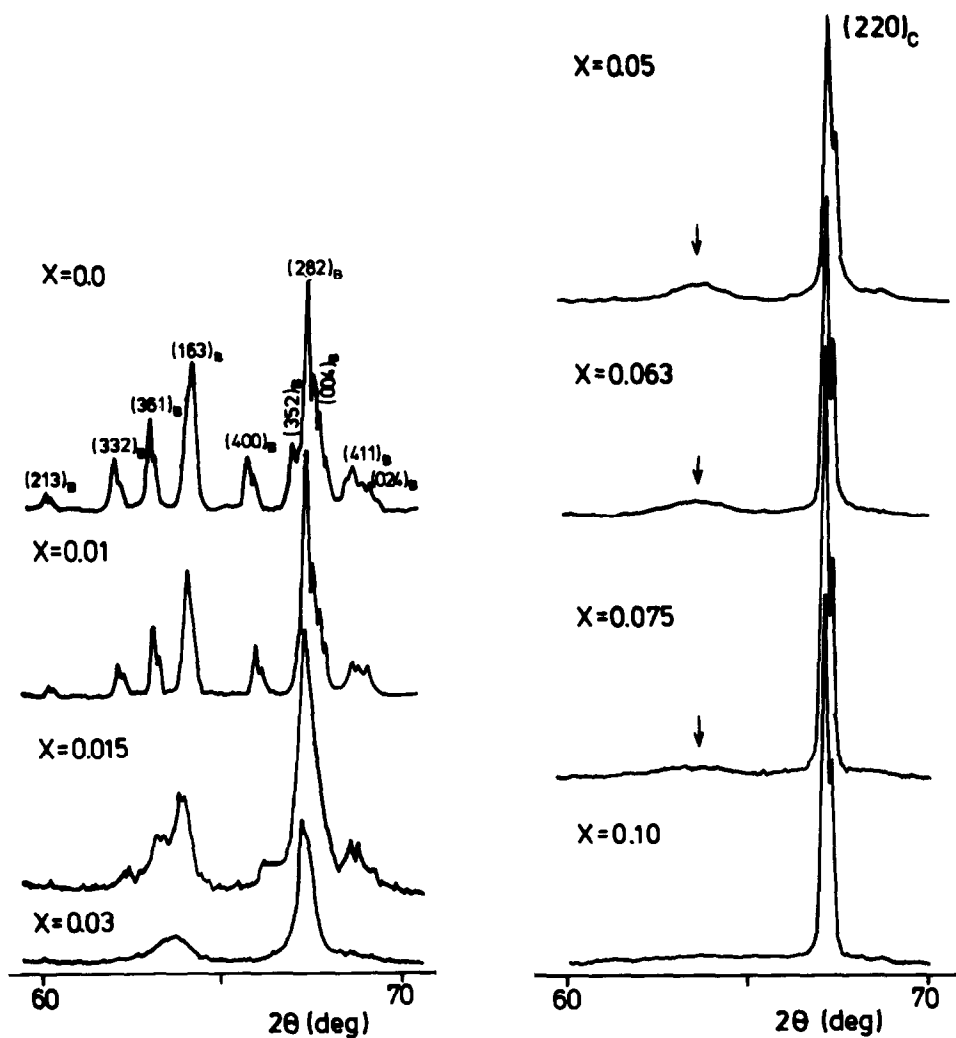
FIG. 1. Variations in the powder X-ray diffraction patterns with composition $x$. Peaks near the (282)$_B$ and (220)$_C$ reflections are shown.

reflections from an impurity phase gave the upper compositional limit of $x$ = 0.10. Thus, we could obtain the cubic perovskite phase for $0.05 \leq x \leq 0.10$. The lattice constant is $a_C$ = 3.934 Å for $x$ = 0.05 and $a_C$ = 3.938 Å for $x$ = 0.10, which are very near the corresponding, pseudo-cubic cell constant of $a_C$ = 3.91 Å for $x$ = 0.0. This "cubic" perovskite phase, however, is characterized by broad peaks as a result of short-range order at positions where the

superlattice reflections of Sr$_2$Fe$_2$O$_5$ appear. Those corresponding to (121)$_B$, (116)$_B$, (222/062)$_B$, and (361/163)$_B$ remain strong enough to be observable. Their FWHM increases as $x$ increases. The crystallographic coherence length calculated from the FWHM of the latter peak by using the Scherrer formula is about 50 Å for $x$ = 0.05 and 20 Å for $x$ = 0.075. Finally, at $x$ = 0.10 these diffuse peaks become too broad to be observed.
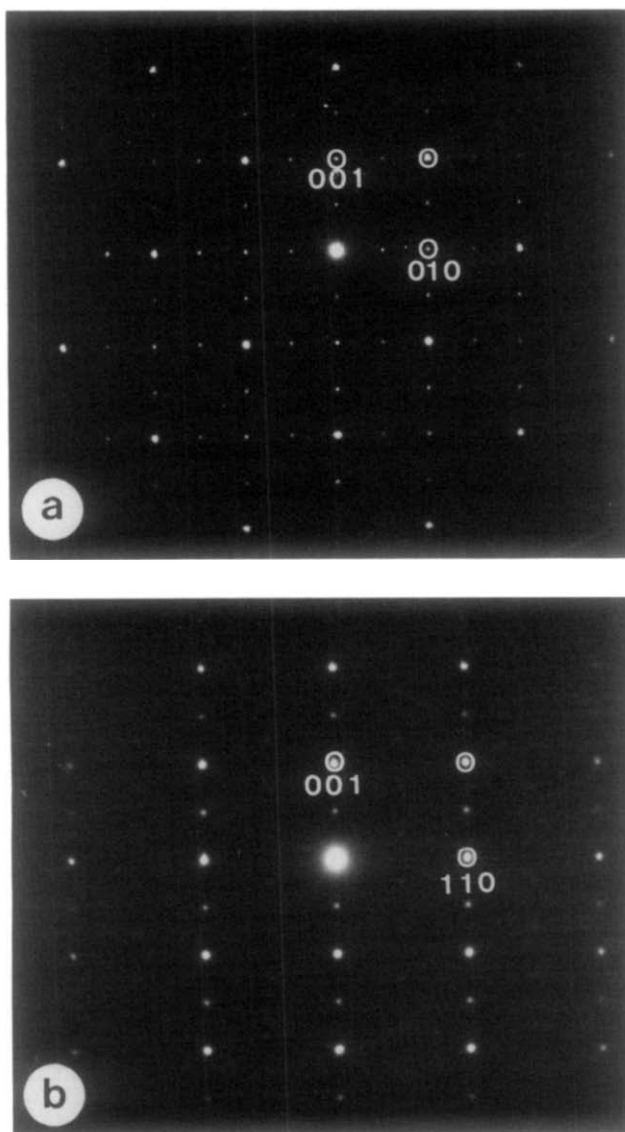
FIG. 2. Typical EDPs of sample $x = 0.05$: (a) $[100]_C$, (b) $[1\bar{1}0]_C$, (c) $[1\bar{2}0]_C$ (d) $[22\bar{1}]_C$. Note the appearance of many superlattice reflections. Some fundamental reflections are indexed.

*Electron Diffraction Patterns*
*and Lattice Images*

Several typical electron diffraction patterns (EDPs) of sample $x = 0.05$ are shown in Fig. 2. In addition to the fundamental reflections expected from the cubic perovskite cell, many superlattice reflections can be seen. The superlattice reflections have been located in the reciprocal space as shown in Fig. 3 from about 10 EDPs with different electron beam incidences. Figure 4 shows some typical EDPs of sample $x = 0.10$. These also show superlattice reflections at the same positions as those for sample $x = 0.05$, though the superlattice
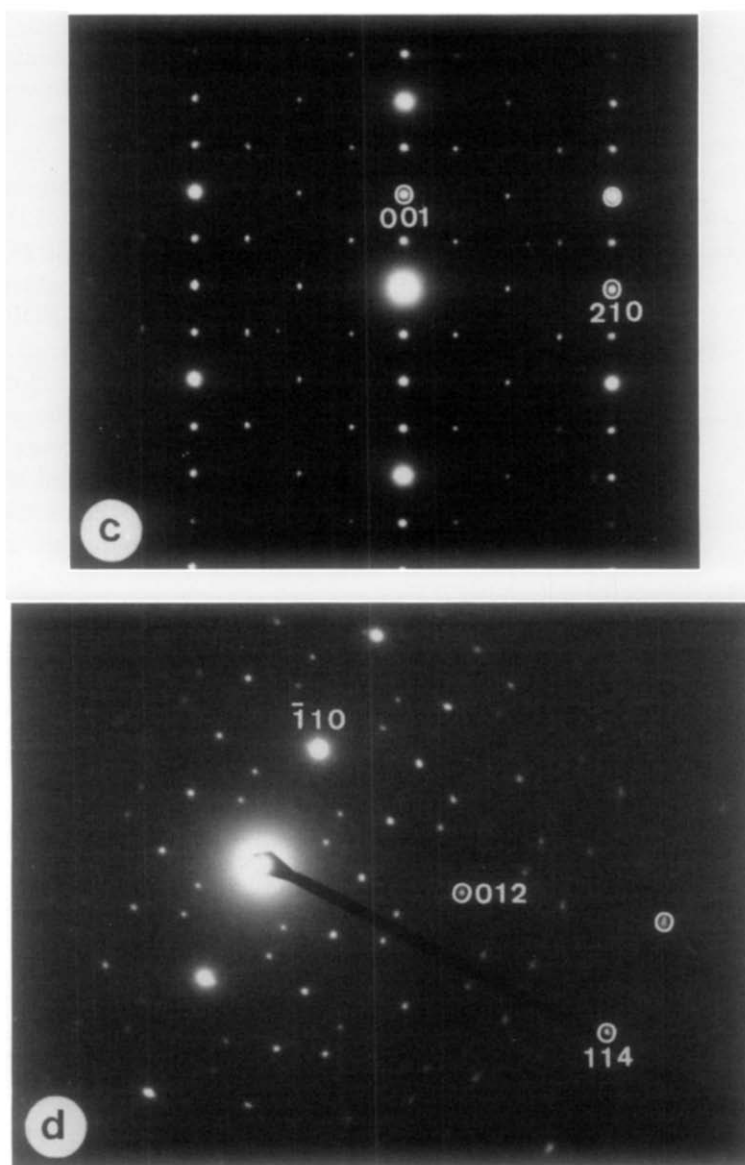
FIG. 2—Continued.

reflections from $x = 0.10$ are weaker and broader. These results are consistent with the XRD observation described in the previous section. It should be noted that the intensities of superlattice reflections are enhanced in these EDPs by using a selected area aperture of about 20 $\mu$m.

Low-magnification lattice images for these two samples are shown in Fig. 5. The incident electron beam is along the $[100]_C$ direction. The corresponding EDPs (Figs. 2a and 4a) indicate a periodicity of $2a_C$ (7.9 Å) along both $[010]_C$ and $[001]_C$ directions. Indeed, the observed images for $x = 0.05$ in Figs. 5a and b consist of lattice fringes with a spacing of 8 Å, but, instead of the crossed
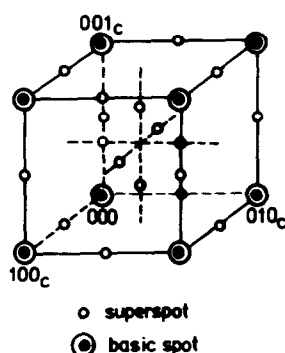
FIG. 3. Positions of the superlattice reflections in the reciprocal space determined from about 10 EDPs with different zone axes.

fringes expected from the EDP, local fringes running parallel to either $[010]_C$ or $[001]_C$ can be distinguished. Moreover, even open areas without fringes can be seen. This indicates that crystals are composed of small domains that crystallize in a certain superstructure on the basis of the cubic perovskite structure but with different orientations. It is reasonable to assume that the domains marked II and III in Fig. 5a give superlattice reflections at $g(0, 0, \frac{1}{2})_C$ and $g(0, \frac{1}{2}, 0)_C$, respectively, and that domain I does not contribute any superlattice reflections. The domain size varies locally from 50 to 200 Å in the case of $x = 0.05$ as compared in Figs. 5a and b. Regions consisting of smaller domains are dominant, and the estimated average domain size of about 60 Å is in good agreement with the coherent length of 50 Å estimated from XRD. The domain size tends to decrease as composition $x$ increases. Although the image for $x = 0.10$ in Fig. 5c also shows lattice fringes with a spacing of 8 Å, they appear wavy and single domains cannot be distinguished.

## Interpretation of EDPs

The preceding observations indicate that the samples of $SrFe_{1-x}V_xO_{2.5+x}$ ($0.05 \leq x \leq 0.10$) are composed of microdomains with a

certain superstructure based on the cubic perovskite. The superstructure has been deduced to be of the brownmillerite type from the following points. In the $[1\bar{1}0]_C$ zone EDP shown in Fig. 2b, the superlattice reflections appear at the same positions as those in the $[001]_B$ zone EDP of $Sr_2Fe_2O_5$ crystallizing in space group $Ibm2$. Also, the $[100]_C$ zone EDP can be obtained by overwriting two $[101]_B$ zone EDPs with mutually orthogonal $[010]_B^*$ axes. As for the orientation of domains, it is clear from the $[100]_C$ zone EDP and the corresponding lattice image that the $b_B$ axes for two types of domains are orthogonal to each other; however, the highly symmetric structure of the parent perovskite leads us to assume the existence of the following orientations:

| | |
|---|---|
| Domain I | $[010]_B//[100]_C, [001]_B//[011]_C$ |
| Domain I' | $[010]_B//[100]_C, [001]_B//[0\bar{1}1]_C$ |
| Domain II | $[010]_B//[010]_C, [001]_B//[\bar{1}01]_C$ |
| Domain II' | $[010]_B//[010]_C, [001]_B//[101]_C$ |
| Domain III | $[010]_B//[001]_C, [001]_B//[110]_C$ |
| Domain III' | $[010]_B//[001]_C, [001]_B//[\bar{1}10]_C$ |

The observed reciprocal lattice diagram shown in Fig. 3 can be reconstructed by overwriting the superlattice reflections from these six kinds of domains. The superlattice reflections arising from each domain and their sum are shown in Fig. 6. The above orientational relation among microdomains in real space can be understood if we return to the cubic perovskite structure and remove the oxide ions to transform it to the brownmillerite structure. As there are six equivalent $\langle 110 \rangle_C$ directions in the cubic system along which vacancies may be stringed, local changes in the string direction from one to another can lead to the above microdomains. All the observed EDPs can be indexed using this microdomain model. The indexing of the EDPs in Fig. 2 is shown in Fig. 7, where superlattice reflections contributed by different domains are differentiated. For example, the $[100]_C$ zone EDP shows superlattice reflections from domains II, II', III, and III'.

Domains II and II' contribute the superlattice reflections at $g(0, \frac{1}{2} + n, m)_C$, while domains III and III' contribute those at $g(0, m, \frac{1}{2} + n)_C$ ($n, m$ = integers). Domains I and I' do not contribute. The corresponding lattice image shown in Fig. 5 reveal only three kinds of domains as the difference

between domains with and without primes cannot be distinguished for this zone axis.

*High-Resolution Lattice Images*

To confirm the microdomain model and to clarify the vacancy ordering scheme within a microdomain, crystallographic co-
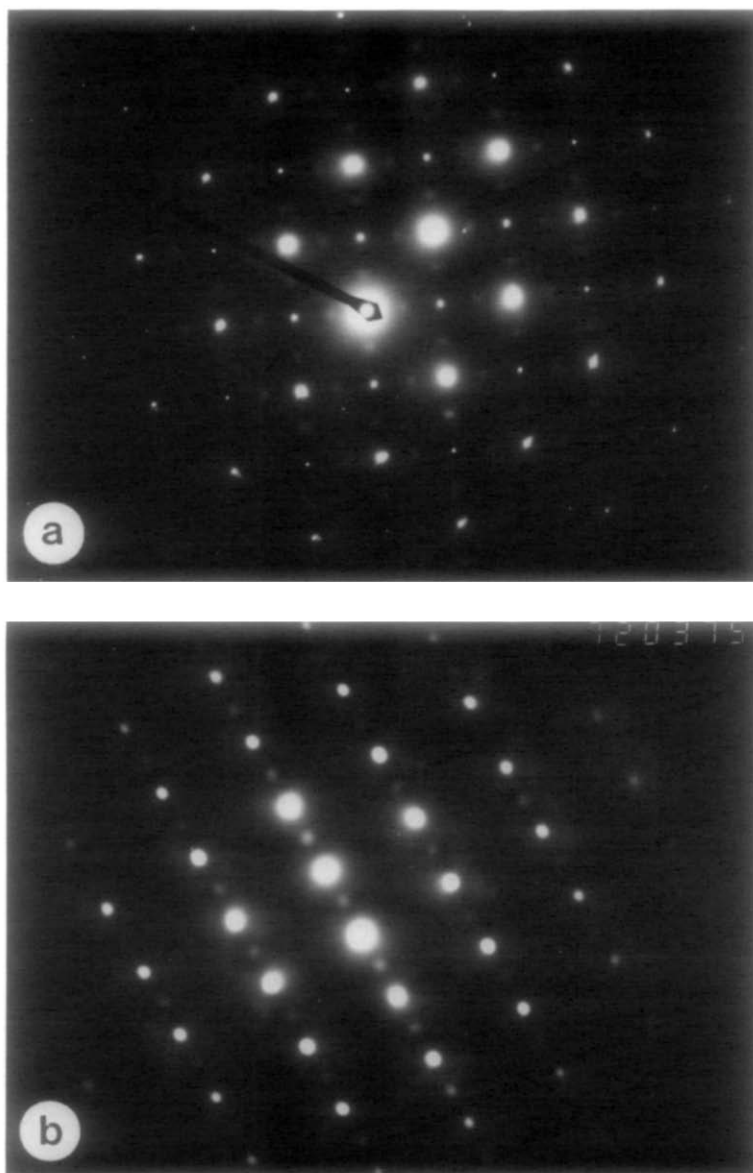


FIG. 4. Typical EDPs of sample $x = 0.10$: (a) [100]$_C$, (b) [110]$_C$. Note the weak and diffuse superlattice reflections.
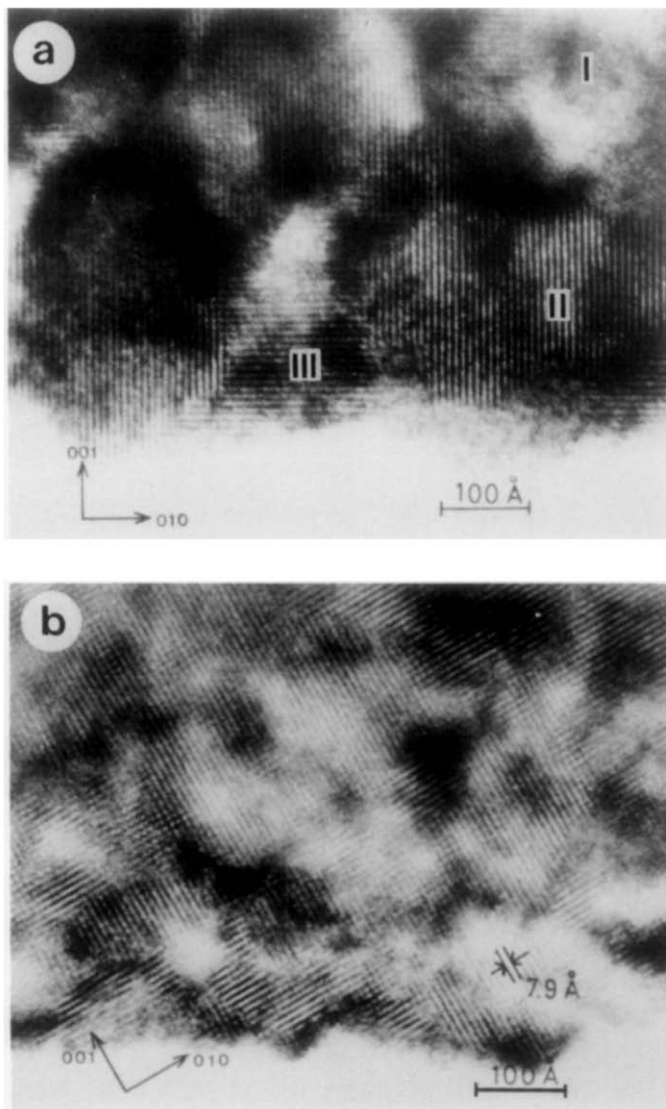
FIG. 5. Low-magnification lattice images of sample $x = 0.05$ (a and b) and $x = 0.10$ (c). The incident electron beam is along the $[100]_C$ direction.

herence between microdomains, and domain boundary structure, high-resolution lattice images were observed. Figure 8 shows a high-resolution lattice image of sample $x = 0.05$. The electron beam incidence is $[110]_C$. It is notable that this direction is parallel to the vacancy string in domain III. The reciprocal lattice and the EDP shown in the Figs. 6 and 7 indicate that the EDP contains superlattice reflections from only two types of domains, III and III'. Both domains III and III' contribute the superlattice reflections at $g(00, \frac{1}{2})_C$. The observed lattice image indeed shows domains with a lattice fringe spacing of 8 Å along $[001]_C$. As the superlattice reflections at $g(\frac{1}{2}, \frac{1}{2}, \frac{1}{4})_C$ arise only from domain III, white dots with a spacing of 5.6 Å appear
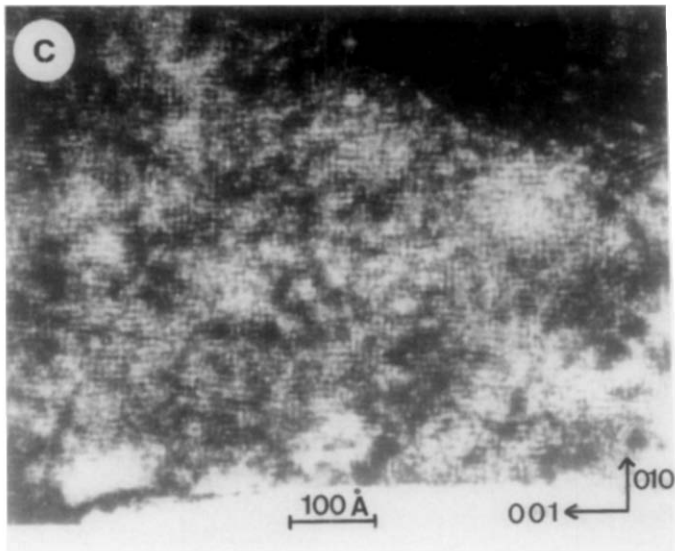
FIG. 5—*Continued.*

along $[1\bar{1}0]_C$ of domain III only. These dots form a planar body-centered lattice and correspond to the arrangement of the vacancy strings. Thus, the vacancy ordering in a microdomain has been confirmed to be of the brownmillerite type.

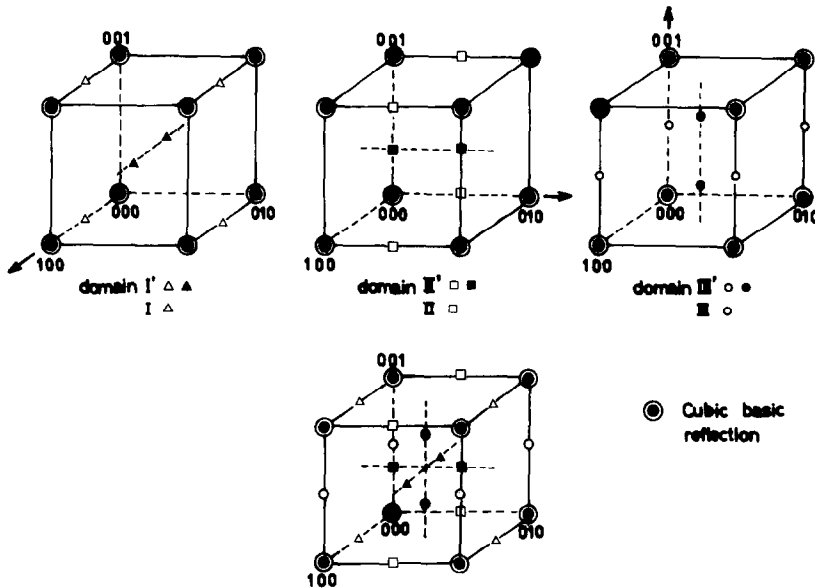It is notable that the basic lattice fringes with a spacing of 2.8 Å along $[1\bar{1}0]_C$ run



FIG. 6. Reciprocal lattice diagram expected for the brownmillerite-type microdomain texture with the six orientation variants. Superlattice reflections contributed by different domains are differentiated.

$[100]_C$

$[1\bar{1}0]_C$
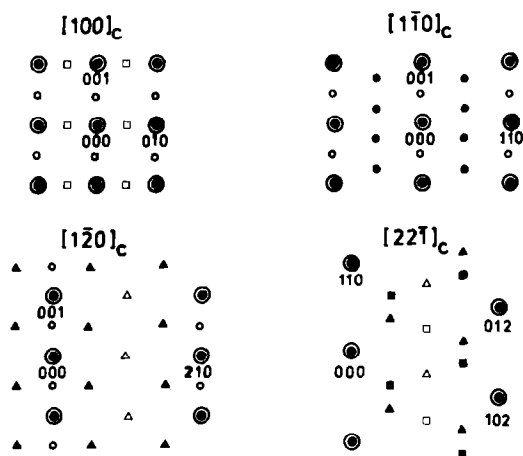
$[1\bar{2}0]_C$

$[22\bar{1}]_C$

FIG. 7. Indexing of EDPs in Fig. 2 using the reciprocal lattice diagram shown in Fig. 6.

without bending from domain to domain. This indicates that the crystallographic coherence between microdomains is fairly good, and can be expected when the vacancy ordering gives atomic shifts (or structural relaxation) much smaller in microdomains than those in $Sr_2Fe_2O_5$. Another important point is that the domain boundaries are neither plane nor stepwise; that is, there are no well-defined twin planes at the boundaries.

Figure 9 shows images of sample $x = 0.05$ taken with the incident electron beam along $[1\bar{2}0]_C$. The EDP contains superlattice reflections from four types of domains, I, I′, III, and III′, as shown in Fig. 7. Domains III and III′ contribute superlattice reflections at $g(2m, m, \frac{1}{2} + n)_C$; domain I′, those at $g(m, \frac{1}{2}m, n)_C$ and $g(\frac{1}{2} + m, \frac{1}{4} + m/2, \frac{1}{2} + n)_C$; and domain I, only those at $g(m, \frac{1}{2} + m, n)_C$ ($m$, $n$ = integers). In the observed images, domains III and III′ can be seen as regions marked with 8-Å-spaced lattice fringes, and domain I′, as regions showing a fine contrast with a periodicity of 3.5 Å along $[210]_C$. On the other hand, domains II and II′ show fringes with a spacing of 3.9 Å along $[001]_C$. Thus, these images are also consistent with the microdomain model.

Good crystallographic coherence and the absence of twin planes at the boundaries can be observed.

Images for sample $x = 0.10$ are shown in Fig. 10. The electron beam incidence is $[100]_C$. Although the low-magnification image shows 8-Å-spaced fringes along both $[010]_C$ and $[001]_C$, these fringes are not localized in separate regions even in the thinnest part of the crystal, making it impossible to identify single domains. In the high-magnification micrograph, however, the basic contrast revealing the perovskite unit cell is modulated by dark or bright 8-Å-spaced fringes running parallel to either $[010]_C$ or $[001]_C$. Outstanding dark or bright fringes are marked in the enlarged image (Fig. 10b). To interpret this interesting image, a computer simulation was made by using the multislice method (12). For simplicity, the composition $Sr_2Fe_2O_5$ was used instead of the real one, $SrFe_{0.9}V_{0.1}O_{2.6}$. Lattice constants of $a = 2^{1/2}a_C$, $b = 4a_C$, and $c = 2^{1/2}a_C$ were used, where $a_C$ is the

TABLE I

PARAMETERS USED IN THE LATTICE IMAGE SIMULATION OF $Sr_2Fe_2O_5$-TYPE MICRODOMAINS SHOWN IN FIG. 11

$Sr_2Fe_2O_5$ lattice constants
$a = 5.564$ Å
$b = 15.736$ Å
$c = 5.564$ Å

Atomic positions in the space group $Ibm2$

|      |       | $x$   | $y$   | $z$   |
|------|-------|-------|-------|-------|
| Sr   | (8c)  | 0.5   | 0.25  | 0.0   |
| Fe1  | (4a)  | 0.0   | 0.0   | 0.0   |
| Fe2  | (4b)  | 0.0   | 0.25  | 0.0   |
| O1   | (8c)  | 0.25  | 0.0   | 0.25  |
| O2   | (8c)  | 0.0   | 0.125 | 0.0   |
| O3   | (4b)  | 0.875 | 0.25  | 0.625 |

Parameters of the electron microscope

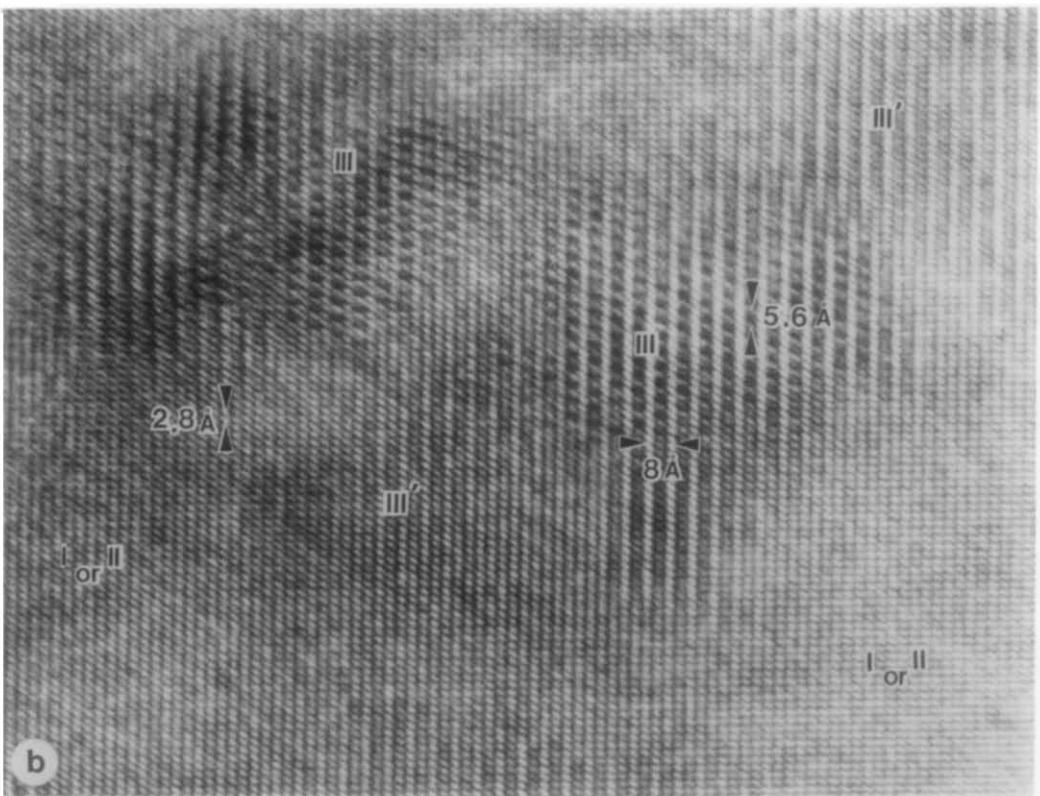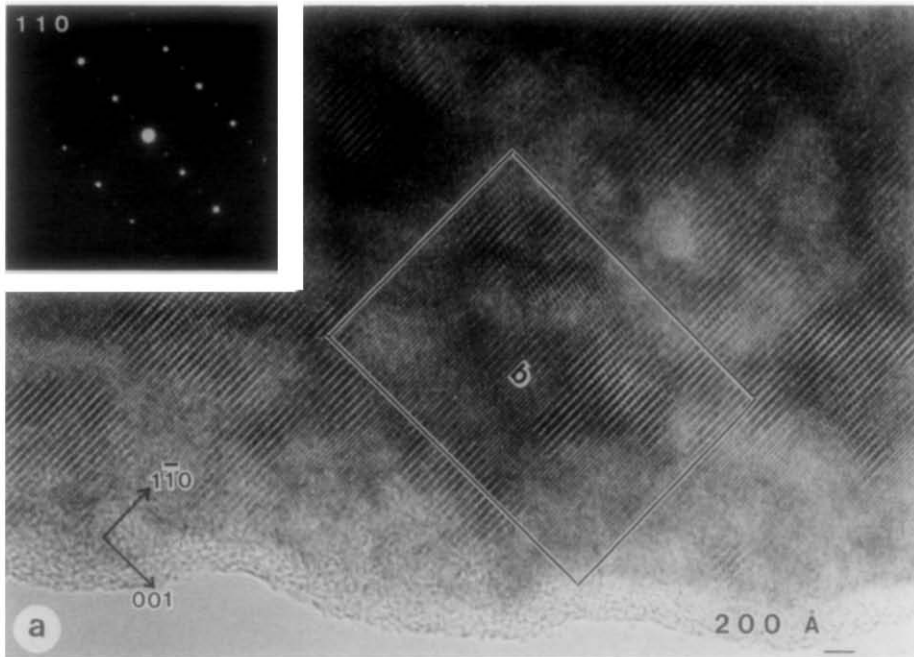| | |
|---|---|
| Objective aperture radius | 0.5 Å$^{-1}$ |
| Spherical aberration coefficient | 1.2 mm |
| Beam divergence | 1.0 milliradian |
| Half-width for depth of focus Gaussian | 50 Å |

FIG. 8. High-resolution lattice images of sample $x = 0.05$. The electron beam incidence is [110]$_C$.
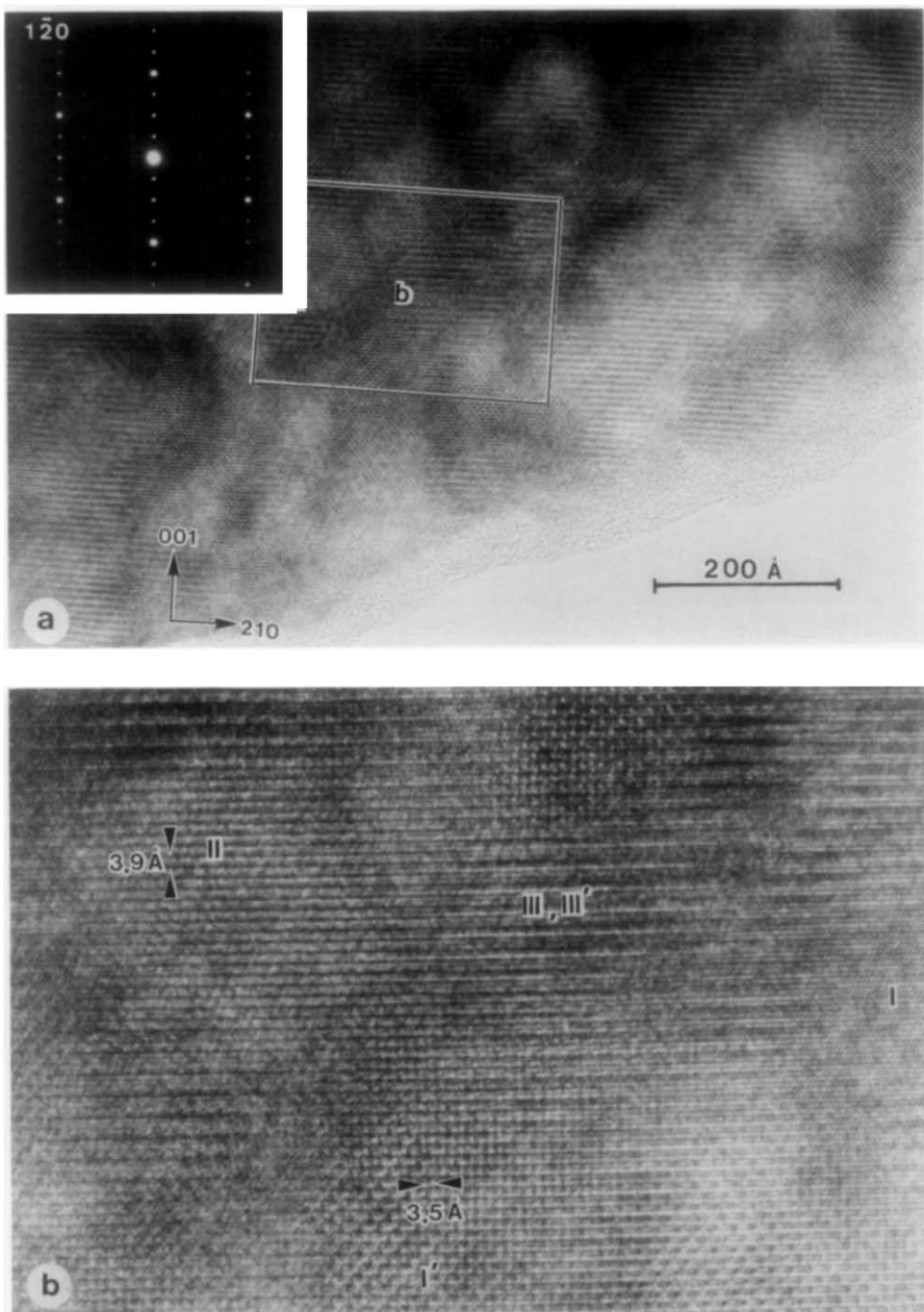
FIG. 9. High-resolution lattice images of sample $x = 0.05$. The electron beam incidence is $[1\bar{2}0]_C$.
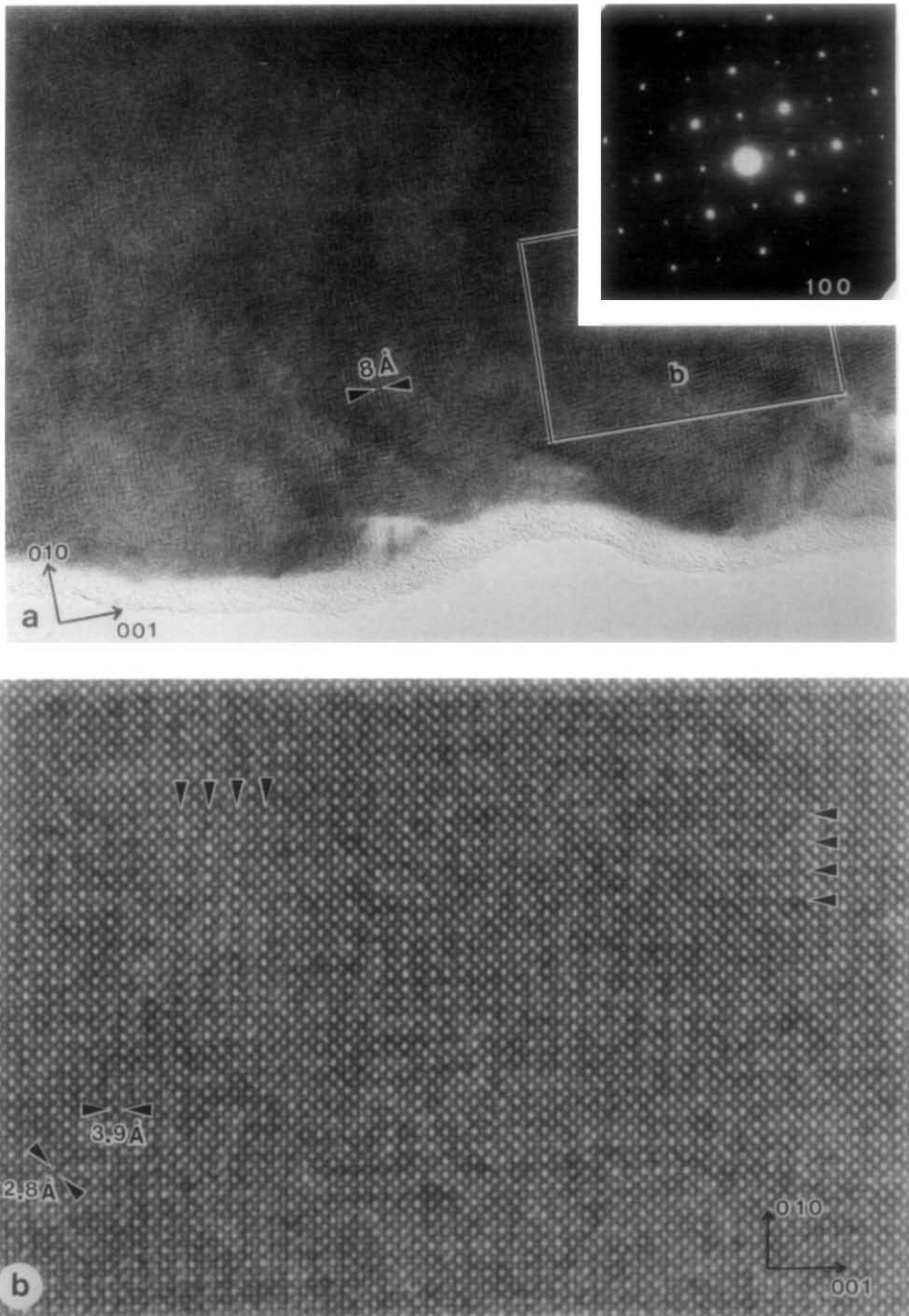
FIG. 10. High-resolution lattice images of sample $x = 0.10$. The electron beam incidence is [100]$_C$. The enlarged micrograph (b) was taken from the enclosed region in (a) but under a different defocus condition.

perovskite cell dimension determined by XRD for sample $x = 0.10$. The atomic positions used are listed in Table I. These were deduced by assuming that the oxygen vacancies are formed in the cubic perovskite structure without affecting the surroundings as suggested from the electron micrographs. The simulated images ($[101]_B$ projection) shown in Fig. 11 reproduce the basic perovskite contrast, with modulating contrasts located at the lattice planes containing vacancies. The modulating contrasts are dark or bright depending on the defocus value. In the experimental micrograph the 8-Å-spaced contrast terminates rather abruptly, indicating that the vacancy ordering is extremely short ranged. This
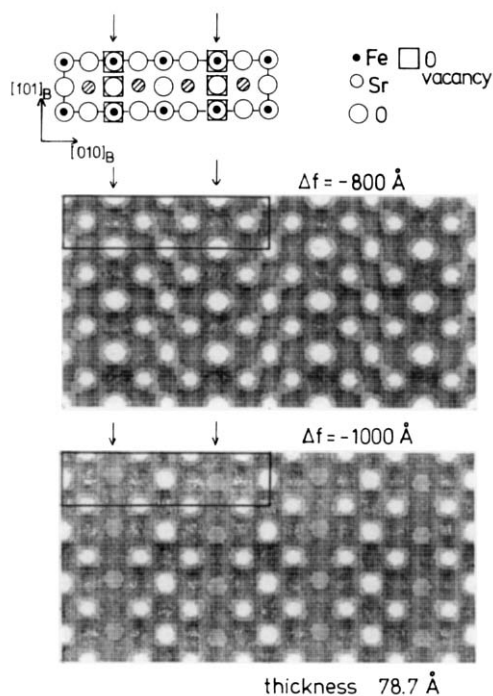


FIG. 11. Calculated images for a brownmillerite-like domain with composition $Sr_2Fe_2O_5$ and the electron beam incidence along the $[101]_B$ direction. Note the contrast at the lattice planes containing oxygen vacancies marked by arrows. These are to be compared with the experimental image in Fig. 10b. The parameters used in the image simulation by the multislice method are shown in Table I.

suggests that a considerable amount of vacancies are disordered. Therefore, the vacancy ordering scheme in this sample may better be considered as clustering.

## Discussion

An underdeveloped vacancy ordering of the brownmillerite type has been observed in the range $0.05 \leq x \leq 0.10$. The extent of ordering strongly depends upon $x$; well-defined microdomains with an average volume of $2 \times 10^5 \, Å^3$ appear for $x = 0.05$, while "vacancy clustering" is appropriate to the state for $x = 0.10$. The good crystallographic coherence among microdomains indicates that underdeveloped ordering causes a structural relaxation of a level much lower than that in $Sr_2Fe_2O_5$. This may be related to the absence of twin planes in the domain boundary regions. The brownmillerite-type ordering within domains, which spares the excess oxygen, and the composition dependence of the domain size strongly suggest that $V^{5+}$ and $O^{2-}$ ions are enriched in the domain boundaries.

Microdomain structure in an oxygen-deficient perovskite has recently been reported for $SrTiO_{2.5}$ (2), $Sr_{1-x}Nd_xFeO_{3-y}$ (3), $Ca_{1-x}La_xFeO_{3-y}$ (4–6), and $CaFe_xMn_{1-x}O_{3-y}$ (7). In comparison with these, the present work shows that the degree of vacancy ordering can be systematically controlled by chemical composition and that the microscopic structure can be observed in great detail.

The oxygen-deficient cubic perovskite phases showing microdomain structure have the following common features. Samples are all rapidly quenched from high temperatures and are microscopically inhomogeneous or two-phase mixtures. In the cases of $SrFe_{1-x}V_xO_{2.5+x}$ and $Ca_2LaFe_3O_{8.273}$ (4), the oxygen concentration at domain boundaries has been suggested to be higher than that in the ordered microdo-

mains. In the cases of $Ca_{0.8}La_{0.2}Fe_{2.665}$ (5) and $CaMn_{1-x}Fe_xO_{3-y}$ (7), two completely different kinds of ordered domains were observed; $Ca_2Fe_2O_5$-type + $Ca_2LaFe_3O_8$-type in the former and $CaMnO_3$-type + $Ca_2Fe_2O_5$-type in the latter. These facts indicate that such a microdomain structure is a quenched early stage of phase separation from a high-temperature disordered phase into two or three mixed phases stabilized at low temperatures. In fact, in the present system, the annealing of sample $x = 0.10$ sealed in an evacuated quartz tube at 673 K for 48 hr was found to destroy the microdomain structure and to give rise to a phase separation into $Sr_2Fe_2O_5$-like and some unknown phases. Also, in the case of the $Ca_{1-x}La_xFeO_{3-y}$ system (13, 14), samples annealed at 1473 K show microscopically disordered intergrowth structure of two different phases.

We present a tentative phase diagram for the $SrFe_{1-x}V_xO_{2.5+x}$ system in Fig. 12. The solubility limit of $Sr_2V_2O_7$ in $Sr_2Fe_2O_5$ is widened at higher temperatures. It is noteworthy that the annealing temperature of 1473 K is higher than the cubic–orthorhombic transition temperature (1123 K) of $Sr_2Fe_2O_5$ (15, 16). By quenching, this cubic phase begins to decompose into $Sr_2Fe_2O_5$ and some unknown V-rich phases, while the domains of the dominant $Sr_2Fe_2O_5$ phase grow in preference. The rapid decrease in temperature and the segregation
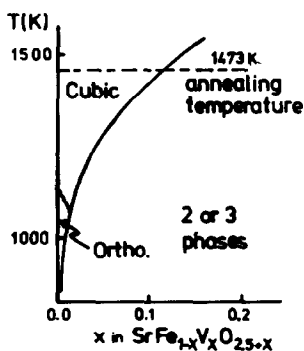
of $V^{5+}$ and excess $O^{2-}$ ions in the boundaries inhibit the growth of $Sr_2Fe_2O_5$ domains throughout the crystals.

## Acknowledgments

## References

1. M. KESTIGIAN, J. G. DICKINSON, AND R. WARD, J. Amer. Chem. Soc. 79, 5598 (1957).
2. M. A. ALARIO-FRANCO AND M. VALLET-REGI, Nature (London) 270, 706 (1977).
3. M. A. ALARIO-FRANCO, J. C. JOUBERT, AND J. P. LEVY, Mater. Res. Bull. 17, 733 (1982).
4. M. A. ALARIO-FRANCO, M. J. R. HENCE, M. VALLET-REGI, J. M. G. CALBET, J. C. GRENIER, A. WATTIAUX, AND P. HAGENMULLER, J. Solid State Chem. 46, 23 (1983).
5. M. A. ALARIO-FRANCO, J. M. GONZALEZ-CALBET, M. VALLET-REGI, AND J. C. GRENIER, J. Solid State Chem. 49, 219 (1983).
6. J. M. GONZALEZ-CALBET, M. VALLET-REGI, AND M. A. ALARIO-FRANCO, J. Solid State Chem. 60, 320 (1985).
7. M. VALLET-RIGI, J. M. GONZALEZ-CALBET, J. VERDE, AND M. A. ALARIO-FRANCO, J. Solid State Chem. 57, 197 (1985).
8. C. GREAVES, A. J. JACOBSON, B. C. TOFIELD, AND B. E. F. FENDER, Acta Crystallogr. B 31, 641 (1975).
9. VON M. HARDER AND H. K. MULLER-BUSCHBAUM, Z. Anorg. Allg. Chem. 464, 169 (1980).
10. S. SHIN, M. YONEMURA, AND H. IKAWA, Mater. Res. Bull. 13, 1017 (1978).
11. S. SHIN AND Y. HATAKEYAMA, Mater. Res. Bull. 14, 133 (1978).
12. P. GOODMAN AND A. F. MOODIE, Acta Crystallogr. A 30, 280 (1974).
13. M. VALLET-RIGI, J. M. GONZALEZ-CALBET, M. A. ALARIO-FRANCO, AND J. C. GRENIER, Mater. Res. Bull. 18, 285, (1983).
14. J. M. GONZALEZ-CALBET, M. VALLET-REGI, M. A. ALARIO-FRANCO, J. C. GRENIER, AND P. HAGENMULLER, J. Solid State Chem. 55, 251 (1984).
15. J. C. GRENIER, N. EA, M. POUCHARD, AND P. HAGENMULLER, J. Solid State Chem. 58, 243 (1984).
16. Y. TAKEDA, K. KANNO, T. TAKADA, O. YAMAMOTO, M. TAKANO, N. NAKAYAMA, AND Y. BANDO, J. Solid State Chem. 63, 237 (1986).

FIG. 12. A tentative phase diagram for the $SrFe_{1-x}V_xO_{2.5+x}$ system.